Surface-Micromachined Electrostatic Deflector for Wide-Band Tunable WDDM Filtering

Yang-Yu Fan[a], Jeffery J. Maki*[b], and Ray T. Chen[a]

[a]Microelectronics Research Center, Department of Electrical and Computing Engineering, The University of Texas at Austin, Austin, TX 78758-4445
[b]Radiant Research, Inc., 3006 Longhorn Blvd., Suite 105, Austin, TX 78758-7631

ABSTRACT

We report a surface-micromachined electrostatic deflector as a controlling element for a novel micro-opto-electro-mechanical (MOEM) bandpass tunable filter for a wavelength-division-multiplexed (WDM) optical-fiber sensor system. Such a tunable MOEM filter involves multiplexed volume holograms, a surface micromachined electrostatic deflector, and an array of Si photodetectors. The micromachined electrostatic deflector, providing fast and repeatable adjustments, greatly enhances the dynamic tuning range of the filter. To micromachine the electrostatic deflector, we use thick (~20 μm) photoresist (AZ9260) as a sacrificial layer that is patterned using conventional microlithography, followed by electroplating. Ten deflectors with different lengths (20 μm in height, 300 μm in width, and 300 to 1200 μm in length) have been fabricated, and the electrostatic actuation of each device has been demonstrated. DuPont photopolymer film is employed for forming multiplexed volume holograms, which in conjunction with a photodetector array will allow the filter to operate at many wavelength windows. The incorporation of the multiplexed volume hologram with the electrostatic deflector will allow us to tune dynamically the filter.

Keywords: surface micromachining, electroplating, microcantilever beam, electrostatic deflector, DuPont photopolymer, holography, multiplexed Bragg gratings, fiber Bragg grating, WDM, WDDM

1. INTRODUCTION

Optical sensors have figured heavily into various sensor systems demonstrated to date. The use of fiber Bragg gratings has become a compelling approach for forming sensors, especially since they can be connected by a common optical data link. The issue is how to make a sensor system based upon them. Demonstrations of sensor systems based on fiber Bragg gratings have been made that use a form of wavelength division multiplexing. In these systems, a tunable laser diode or a tunable acousto-optic filter[1,2,3] outputs a particular narrow-bandwidth optical wave at a given time that has the correct wavelength to probe a given sensor along the optical fiber of the link or interconnect. The sensor modifies the reflection for this wavelength and thus creates a signal wave to be detected at the output of the fiber link. Other sensors are then selected by changing the probe wavelength. The problem with using a tunable laser diode is that a large wavelength tuning range is not currently available, whereas the problem with tunable acousto-optic filters is that they are bulky and simply not suitable for use in an integrated fiber-optic-sensor network. Other limitations of tunable laser diodes and tunable acousto-optic filters include high drive power, poor reliability, and high cost.

In contrast to any existing approach, we propose a novel micro-opto-electro-mechanical (MOEM) device for wavelength division demultiplexing (WDDM) simultaneous signals coming from all of the sensors, which are each based upon fiber Bragg gratings. This tunable MOEM demultiplexer, as shown in Fig. 1(a) and 1(b), involves a thin-film multiplexed volume hologram, an electrostatic-actuated microcantilever beam, and a Si photodetector array. The fabrication is by surface micromachining on a standard semiconductor wafer. The number of channels that can be demultiplexed is increased by the electrostatic-actuated microcantilever, which provides fast and repeatable adjustments of the angular orientation of the hologram. An applied voltage adjusts the difference in the charge placed across two parallel-plate electrodes, which controls the amount of electrostatic actuation. The use of a multiplexed volume hologram in conjunction with a

*Correspondence—Email: maki@radiantr.com; WWW: http://www.radiantr.com; Telephone: 512-339-0500 ext. 203; Fax: 512-339-1311

Part of the SPIE Conference on Optoelectronic Interconnects VI
San Jose, California • January 1999
SPIE Vol. 3632 • 0277-786X/99/$10.00

photodetector array allows the MOEM demultiplexer to operate at many simultaneous wavelength windows such as 633 nm, 670 nm, 850 nm, 980 nm, 1300 nm, and 1550 nm. Multiplexing the output of the various individual sources and then coupling them into a fiber-optic cable forms a single optical source. The choice of a semiconductor such as Si, GaAs, or InP as the substrate material allows the incorporation of a photodetector array and drive electronics on the same chip.

Shown in Fig. 1(c) is the proposed sensor system. In a fully integrated system, a large number of fiber Bragg-grating sensors are wavelength division multiplexed (WDM), distributed by fiber-optic data link, and then wavelength division demultiplexed (WDDM) by the proposed integrated MOEM device, where only a single light source (depicted by a broadband LED) is required. In Fig. 1(c), each Bragg grating in the distributed fiber sensor network reflects a specific wavelength within the bandwidth of the light source. These reflected sensing signals, having different wavelengths, are collected by a fiber coupler and delivered to the proposed MOEM device. A gradient index (GRIN) lens collimates and focuses the input beam derived from the output of the fiber-optic data-link cable. A list of measurands for such a sensor network includes temperature, strain, pressure, displacement, rotation, etc.

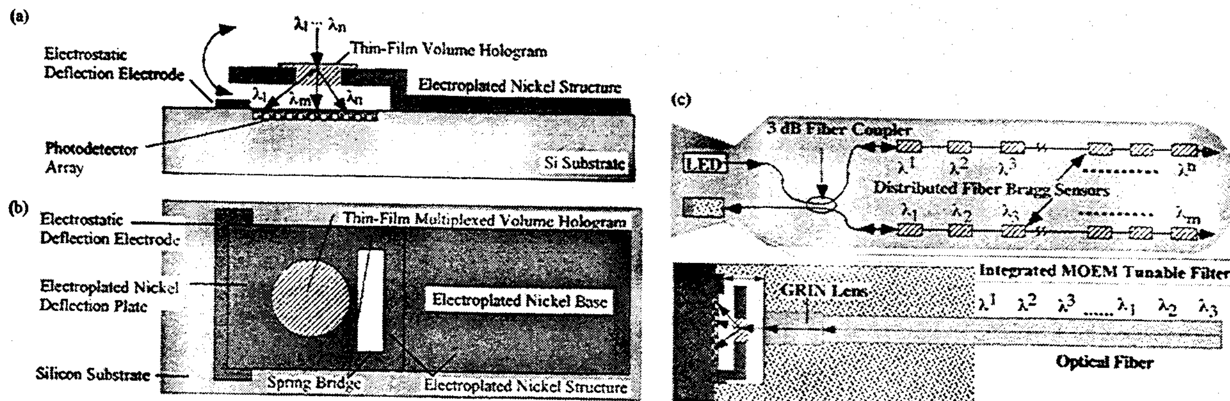

FIG. 1. (a) Side view and (b) top view of the MOEM device. (c) Bragg-grating sensor system with proposed MOEM tunable filter.

The feasibility of this proposed MOEM tunable filter depends mainly on the demonstration of the electrostatic deflector, multiplexed thin-film volume hologram for multi-channel operation, and the integration of them. In Sec. 2, we will first discuss the design concept of the proposed MOEM tunable filter incorporated into the sensor system. Since the surface-micromachined electrostatic deflector is the emphasis of this paper, in Sec. 3 to 6, a complete discussion of the fabrication process will be made and followed by demonstration of micro-actuation. In addition, the multiplexed thin-film volume hologram for multi-band operation will be demonstrated in Sec. 7.

2. DESIGN CONCEPT OF MOEM TUNABLE FILTER

A more detailed illustration of the MOEM device is shown in Fig. 2 to make clear the essential operation of the tunable filter. For clarity, only two of the many photodetector elements of the photodetector array are depicted. Furthermore, we depict the action of only two of the several multiplexed Bragg gratings that are within the volume hologram. Assume the multiplexed signal (input) beam has individual signals centered at wavelengths of 630 nm and 800 nm. One of the two multiplexed holograms diffracts by ~45° the light centered at 630 nm, whereas the other multiplexed hologram diffracts by ~30° the light centered at 800 nm. The ~800 nm light is not Bragg matched for diffraction by the grating designed to diffract light by ~45°, and similarly the ~630 nm light is not Bragg matched for diffraction by the grating designed to diffract light by ~30°. The ability to multiplex Bragg-gratings within the volume of the photopolymer film, by using holography, provides for the wide dynamic range of the MOEM demultiplexer. The multiplexed hologram provides for the simultaneous diffraction of two very different wavelength bands at design-specified angles, but furthermore the nature of diffraction by a Bragg grating eliminates the unwanted multiple orders of diffraction that a traditional diffraction grating produces even with blazing, such as which occurs in a scanning monochromater. The placement of the two detector elements provides for detection of light diffracted by ~30° and ~45° with respect to the surface normal of the silicon substrate housing the detector array. Shown in Fib. 2(a), for no tilting of the cantilever (i.e., $\theta_{tilt} = 0$), one of the Bragg gratings diffracts 630-nm light at 45° (dashed line), >630-nm light at >45° (dashed line), and <630-nm light at <45° (solid line). The solid line

indicates that for this angular orientation (i.e., $\theta_{tilt} = 0$) only light within this subband is diffracted with appreciable efficiency.

When a voltage is applied, the tip of the cantilever beam pulls down owing to the attractive electrostatic force, which causes the cantilever beam to bend as depicted in Fig. 2(b). For a specified DC bias voltage, the cantilever beam bends and thus tilts the multiplexed hologram to its nominal angular orientation, which is $\theta_{tilt} = \theta_{tilt0}$. At this nominal tilt angle, the center wavelength of 630 nm is diffracted with appreciable efficiency and incident upon the detector 1. An increased applied voltage would then cause detection of the even redder wavelength subband or channel. Hence, the bandpass of the MOEM demultiplexer is tuned to select various channels that correspond to various fiber Bragg-grating sensors.

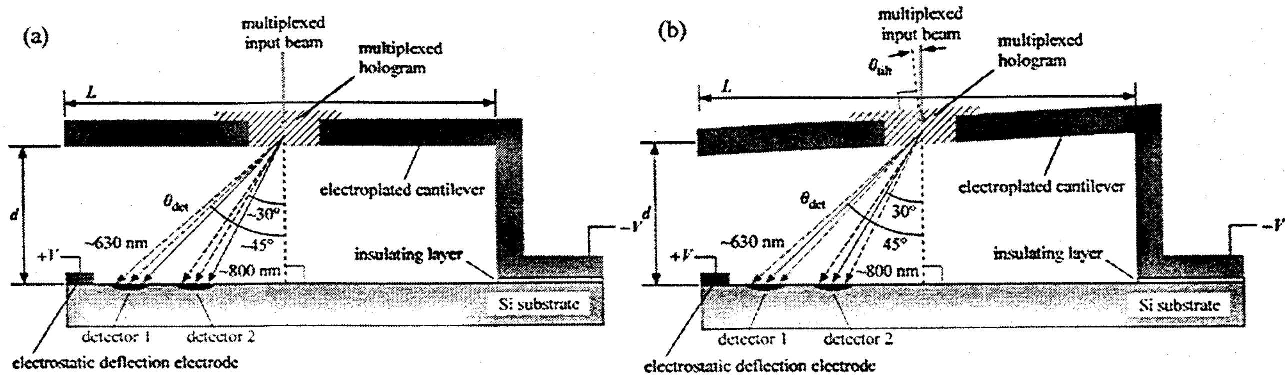

FIG. 2. (a) Detailed MOEM tunable-filter concept. (b) Electrostatic actuation of the microcantilever beam tunes the MOEM filter and thereby selects a specific subband that is detected by a given detector element in the detector array; and thus the signal from a specific Bragg-grating sensor is demultiplexed.

3. ELECTROSTATIC-ACTUATED CANTILEVER

The electrostatic force is the primary force used to give life to micromachined devices. The force is used to change the bending angle of microcantilever beams, to modify the shape of microbridges, or to engage a microbrake to halt or prevent motion. The electrostatic force is the attractive force that occurs between two metal plates that carry opposite charge, which occurs when a voltage is applied across them. This force scales inversely with the square of the distance between the plates. The electrostatic force thus becomes significant for microstructures owing to the small distance between the electrode plates and the small mass of the moving parts. Also, because of the small mass, the force due to gravity becomes insignificant. The other force involved that is significant is the spring-like restoring force of metals or other materials that causes them to return to their original shape. All of these attributes provide for micromachined parts to have interesting applications over their macroscopic counterparts.

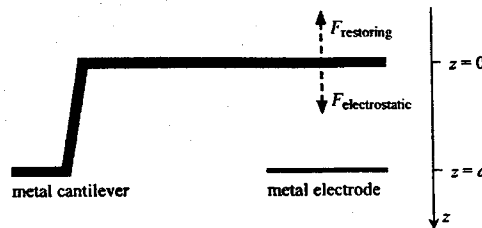

FIG. 3. Forces determining the position of the tip of a metal cantilever beam along the z–axis.

Figure 3 illustrates the forces that control the bending of a cantilever beam. The metal cantilever and the metal plate a distance *d* away form opposing plates like in a capacitor. The application of a voltage *V* causes the attractive force

$$F_{electrostatic} = \frac{\varepsilon_0 A}{2}\left(\frac{V}{d-z}\right)^2 \tag{3.1}$$

to occur between the metal plates, where $\varepsilon_{\circ}$ is the permittivity of air and A is the area between the plates. The restoring force is simply

$$F_{\text{restoring}} = -k_{\text{spring}} z \,, \tag{3.2}$$

where k_{spring} is the spring constant for the hinge of the cantilever beam. Basic properties of the nature of electrostatic actuation are realized by plotting (see Fig. 4) the potential energy

$$U(z) = -\int \left(F_{\text{electrostatic}} + F_{\text{spring}}\right) dz = \frac{1}{2} k_{\text{spring}} z^2 - \frac{\varepsilon_0 A}{2} \left(\frac{V}{d-z}\right) \tag{3.3}$$

of the cantilever beam as a function of the position of the tip of the cantilever beam along the z–axis. For increasing applied voltage, the range of stable positions decreases, where the steady state position is at the bottom of the potential well. At a certain applied voltage, no potential well remains, there is no longer a stable intermediate position for the cantilever, and z increases until the cantilever touches the other electrode. The runaway strength of the electrostatic force causes the beam to make physical contact with the bottom electrode abruptly in time and is known as clamping. Therefore, the electrostatic force can only be used to cause actuation of the microcantilever beam over a limited range of displacements Δd as depicted in Fig. 5.

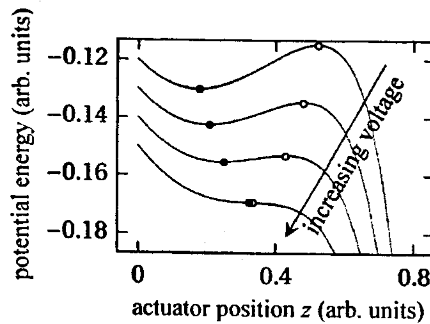

FIG. 4. Potential energy diagram of the bent cantilever beam, where the solid circles are the equilibrium positions and the open circles are the maximum possible actuator displacements without runaway displacement that would cause the cantilever to clamp to the bottom electrode.

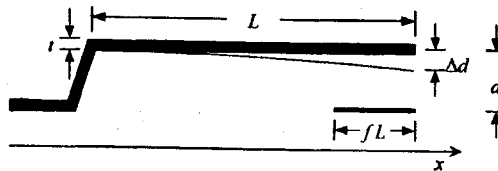

FIG. 5. Specific geometry of the cantilever beam and bottom electrode.

To investigate the influence of the size and position of the bottom electrode, we follow the theoretical approach of Petersen.[4] The essential aspects of the approach are given as follows. A concentrated differential element of load/force, $bq(x)dx$, at a position x on a uniform cantilever beam results in a deflection at the tip of the beam,[5] which is

$$d\delta_{\text{T}} = \frac{x^2}{6EI}(3L - x) bq(x) dx \,, \tag{3.4}$$

where Y is Young's modulus, I is the moment of inertia, b is the width, and L is the length of the cantilever beam. The total deflection of the tip is found by integrating Eq. (3.4) over the range of x values that the bottom electrode is located. Integrating over this limit range is an extension of the result given in Ref. 4. The equation for this is

$$\delta_T = \frac{b}{6EI}\int_{(1-f)L}^{L}(3L-x)x^2 q(x)dx \ . \tag{3.5}$$

The electrostatic force per unit area is

$$q(x) = \frac{\varepsilon_0}{2}\left(\frac{V}{d-\delta(x)}\right)^2 \ . \tag{3.6}$$

To know the force, however, one must know the position of the deflected beam, which is what we are trying to solve and thus do not know. We use an approximate equation that describes the shape of the deflected beam in terms of the displacement of the tip of the cantilever beam. We use

$$\delta(x) \cong \delta_T\left(\frac{x}{L}\right)^2 \ . \tag{3.7}$$

The combination of Eqs. (3.5) through (3.7) and the substitution $\delta_T = \Delta\, d$ yields

$$V = V_0\sqrt{\frac{6\Delta}{\int_{1-f}^{1}\frac{(3-\bar{x})\bar{x}^2 d\bar{x}}{(1-\bar{x}^2\Delta)^2}}} \ , \tag{3.8}$$

where the parameter scaling the voltage is

$$V_0 = \sqrt{\frac{2EId^3}{\varepsilon_0 bL^4}} \ . \tag{3.9}$$

Figure 6 shows a plot of Eq. (3.8) for various lengths of the bottom electrode, where for $f = 1$ the bottom electrode is as long as the cantilever beam and for $f = 0$ the bottom electrode is absent. One can immediately see that reducing the length of the bottom electrode to one tenth of the length of the top electrode (i.e., $f = 0.1$) increases the voltage required to reach a given deflection by only about a factor of two. Thus limiting the length of the bottom electrode to accommodate the placement of the photodetector array does not severely limit the operation of the electrostatic microcantilever.

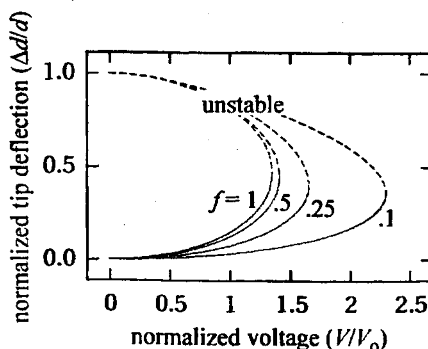

Fig. 6. Stability analysis of the tip deflection with applied voltage. The dashed lines are the unstable values of the tip deflection.

We now examine some specific geometries to predict the voltage required by the microcantilever and the amount of tilting the microcantilever will be able to provide. To this end, we use a model[4] for the moment of inertia is $I = bt^3/12$, which gives

$$V_0 = \sqrt{\frac{Et^3d^3}{6\varepsilon_0 L^4}} \quad . \tag{3.10}$$

Note that the width b of the cantilever beam no longer appears in the formula for V_0. For Nickel,[6] Young's modulus Y is 2.1×10^{11} Pa. We also take $t = 2$ μm and $d = 20$ μm. The tilt angle is computed using $\theta_{tilt} = \tan^{-1}(L/2\Delta d)$, where Δ is given implicitly by Eq. (3.8). Shown in Fig. 7 is the maximum value of the tilt angle θ_{tilt} that can be reached before clamping, where the length of the bottom electrode scales with the length L of the cantilever beam according to $L/4$. Figure 8 gives the predicted operation of a cantilever beam with varying voltage that has a length $L = 400$ μm. In summary, electrostatic actuation of microcantilever beams can tilt a structure, such as the planned multiplexed holographic element, by about a degree or two for reasonable values of the applied voltage.

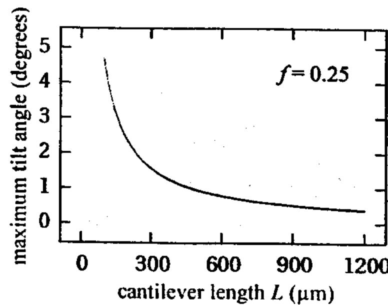

Fig. 7. Maximum tilt angle of a cantilever beam plotted as a function of its length assuming the thickness t is 2 μm and the height d is 20 μm.

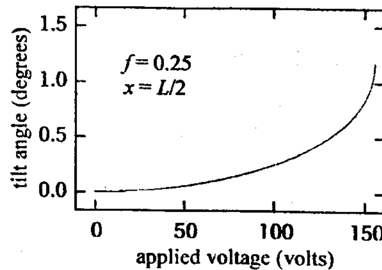

Fig. 8. Tilt angle of a nickel cantilever beam that is 2 μm in thickness t, 20 μm in height d, and 400 μm in length L.

4. FABRICATION OF MICRO-DEFLECTOR

The approach we use to fabricate the metal micro-deflector beam is surface micromachining. The major advantage of surface micromachining, compared to bulk micromachining, is there is no practical limit to how small the device can be. In our process, which is outlined in Fig. 9, we use thick (20 μm) positive photoresist (AZ9260) as a sacrificial layer that is patterned using conventional microlithography. Then, chromium (Cr) and gold (Au) are deposited as the seed layer for electroplating. After nickel (Ni) is plated to complete the structure, the sacrificial layer is removed by photoresist stripper (e.g. AZ 400T).

We micromachine the micro-deflector upon a silicon substrate that is predeposited with a layer of silicon dioxide. The choice of substrate has no restriction, as long as an insulating layer can be predeposited to make all metal structure patterned on this insulating layer are electrically isolated. A layer of 300 Å chromium and a layer of 800 Å gold are first deposited uniformly on top of the substrate by an electron-beam evaporator. Then the base electrode is fabricated by photolithography.

The next step is to spin coat and pattern a layer of thick photoresist (AZ9260) on the substrate, which is called the sacrificial layer. This layer of thick photoresist will remain during the remainder of machining, but will eventually be re-

moved. Using this sacrificial layer, the spatial separation between the surface of the substrate and the bottom surface of the micro-actuator is defined. By a two-step spin-coating procedure, a 20-μm layer of AZ9260 is placed on a Si substrate.

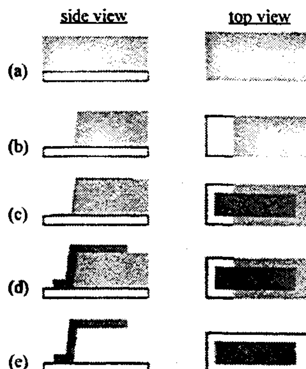

FIG. 9. Overview of the fabrication procedure for making a microcantilever beam by electroplating nickel over the edge of a thick sacrificial film of photoresist, which is later dissolved away.

The final major clean-room step is preparation of the metal seed structure for electroplating the cantilevers. We again use an electron-beam evaporator to deposit chromium and gold over the entire surface of the substrate. Then photolithography is used to produce the seed-layer pattern that defines the length and width of the micro-deflector. This process deviates from the conventional one owing to the sensitive property of the thick AZ9260 photoresist. One problem is the adhesion between the AZ9260 layer and the metal layer as well as the surface tension of the top metal layer. The chromium placed on top of the AZ9260 not only acts as a glue layer, but also acts as a buffer layer between the AZ9260 and the gold. Another problem is that during metal deposition the surface temperature will increase and cause the metal to crack as a result of the different thermal expansion coefficients. To alleviate this problem, the sample is first hard baked at 112°C for 30 min. This step (1) reduces the surface tension inside the photoresist and (2) reduces the effect of thermal expansion during metal deposition. The malleable property of gold makes it an ideal choice. In addition, the thickness should be limited to the smallest useful thickness owing to the progressive increase in the temperature of the sample that occurs with continued metal deposition. We found that optimum thickness of gold is 1100 Å.

After metal deposition, we use conventional photolithography to pattern the metal layer into the specific cantilever seed structure. A layer of photoresist (e.g. AZ5209) is first spin cast. The next step is to soft bake at 90°C for 10 to 30 minutes to remove the residue solvent and release any residual strain in the photoresist layer. For most cases, this passivation step ensures that the photolithography will yield a properly patterned photoresist layer, where the dimensions are controlled precisely. In our case, though, this step will cause too much thermal expansion of the underlying sacrificial layer and cause the sacrificial layer to break the metal deflector-seed structure at the location of the hinge. Due to the large feature size of our device (i.e., >300 μm), the soft-bake step can be eliminated or, at least, the soft bake time can be greatly reduced, where we forgo precise control of the feature size. However, contact-mask printing requires that the surface is free of any moisture or any excess solvent, so we use a relatively quick soft bake (about 10 sec) before UV exposure. In addition, the hard bake before metal etching is skipped for the same reason.

There is also a problem relating to the removal of the photoresist after metal etching. Acetone or any other strong chemical etchent cannot be applied since the bottom sacrificial layer would be removed at the same time. Two possible schemes circumvent this problem. In the first scheme, the sample is UV-flood exposed, rinsed with a developer (i.e., AZ425) that has a slow etch rate for the thick sacrificial layer made of AZ9260. Then, reactive oxygen-ion etching removes any residual photoresist.

The gold seed layer is then Nickel electroplated following standard methods. The sacrificial layer, though, is no longer needed and may be removed to release the finished micro-cantilever beams. The sacrificial layer must be removed carefully so as not to distort or damage the cantilever beams. We make use of the slow etch rate of developer realizing that a quick etch rate may cause the cantilevers to peel off. After the developer has removed most of the sacrificial layer, we place the sample in stripper to remove any residual photoresist that may remain at the hinges of the cantilevers. The stripper has a quick etch rate, but is of no consequence since there are only very small deposits of photoresist that remain after

the use of the developer. The detailed procedure we use it to (1) UV-Flood expose; (2) rinse in AZ400K developer; (3) rinse in AZ400T stripper; (4) rinse in deionized water; and (5) hard bake at 112°C to remove any water. In Fig. 10, we present three of the fabricated micro-deflectors, each has 300 μm in width, 20 μm in height, but different lengths.

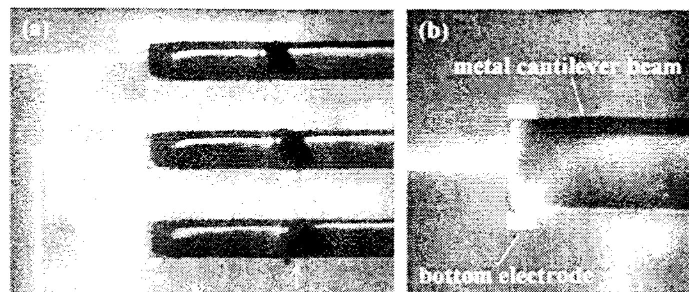

Fig. 10. (a) Close-up of three of the ten microcantilevers beams, where the arrows mark the positions of the hinges of the progressively longer cantilever beams. (b) Extreme close-up showing the exposed bottom gold electrode and the top electrode provided by the nickel-electroplated microcantilever beam.

The thickness and shape variation of the cantilever beams is determined by the detailed nature of the electroplating process. The overall metal thickness steadily increases as the sample remains in the electroplating bath with current applied. The conductivity of the metal seed structure and the uniformity of the voltage applied over the seed structure influence the shape of the resulting cantilever beams. Note that in electroplating the metal deposition rate follows the current density across the surface of the sample. No metal deposition occurs in any area of the sample where current cannot flow.

5. MEASUREMENT OF ELECTROSTATIC ACTUATION OF MICRODEFLECTOR

We have performed measurements of the electrostatic actuation of our micro-deflector beams fabricated by metal electroplating. Our method for measuring the angular actuation of the cantilever beams is illustrated in Fig. 11. We determine the amount of microcantilever beam bending (i.e., θ_{tilt}) by monitoring the angle of reflection of a laser beam that is incident on the top shiny surface of a metal cantilever beam. The reflected beam of a HeNe laser is easily viewed by eye. We place a screen in the path of the reflected laser beam. We monitor the displacement of the laser beam striking the screen as the voltage is varied across the metal cantilever and the bottom metal electrode. This displacement divided by the distance from the cantilever to the screen is converted into the angle of deflection of the beam.

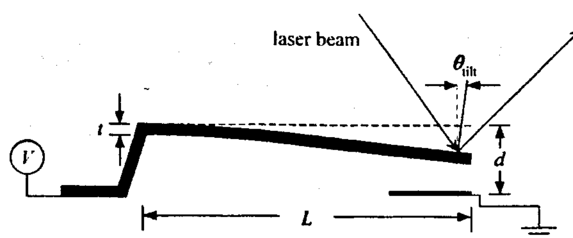

Fig. 11. Schematic drawing of the measurement scheme for determining the amount of bending (i.e., θ_{tilt}) of the microcantilever beam.

Shown in Fig. 12 are the measurements for the laser-beam deflection angle plotted as a function of the applied voltage. The deflection angle increases with the applied voltage. The amount of deflection is not linear with the applied voltage. Higher values of the applied voltage cause much larger deflection angles. Recall that in Sec. 3 we presented a model for an electrostatically actuated cantilever beam. Figure 8 gives predictions for the angular tilt with applied voltage. The shape of the curve in Fig. 8 is very similar to the measured curves shown in Fig. 12.

We show the results for cantilever beams of 5 different lengths L, which is defined in Fig. 11. The specific lengths L are noted in Fig. 12. One can see that the longer cantilevers produce a larger deflection for the same value of the applied voltage compared to the shorter cantilever beams. Equation (3.10) gives the characteristic voltage for the cantilever actuation, which shows that the required voltage to drive a cantilever scales according to

$$V_0 \propto \frac{t^{\frac{3}{2}} d^{\frac{3}{2}}}{L^2} \ . \tag{5.1}$$

Thus, the general trend is that the voltage required producing a given amount of angular actuation decreases as the cantilever length is increased. The data reported in Fig. 12 supports this reduction in the required voltage with increasing cantilever length. The metal cantilevers have a thickness t (defined in Fig. 11) that is approximately 15 μm. Equation (5.1) shows that the required voltage would drop by $(2/15)^{\frac{3}{2}} \cong 1/20$ if the thickness were reduced to 2 μm. Hence, the 225 V used to yield the approximately 1° of angular actuation for the 1100 μm cantilever is predicted to reduce to 11 V.

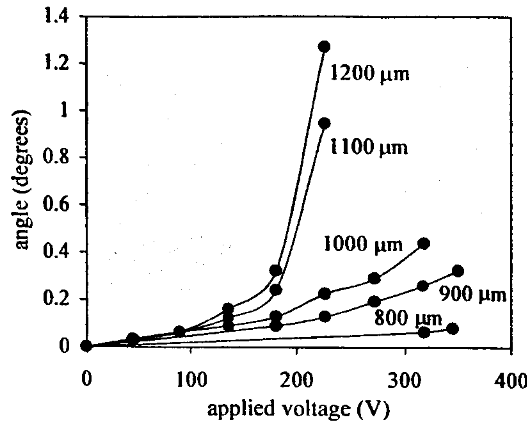

Fig. 12. Plotted as a function of the applied voltage is the measured angle of deflection for 5 different microcantilever beams, with different lengths of 800 μm to 1200 μm.

In summary, microcantilever beams, which have been fabricated by microlithography and electroplating techniques, demonstrate electrostatically driven angular actuation.

6. MULTI-BAND OPERATION

In our MOEM device, we employ DuPont photopolymer to form multiplexed Bragg gratings using holographic recording methods. The multiplexed Bragg gratings are used to separate the optical signals of different wavelength bands. The following is a discussion of the multiplexed thin-film volume hologram for multi-band operation.

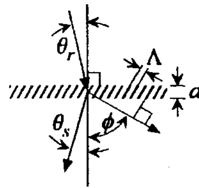

Fig. 13. Light incident at an angle θ_r is diffracted at an angle θ_s by a Bragg-grating with period Λ that is oriented at an angle ϕ.

The key aspect of a Bragg grating is the elimination of the many diffracted orders that occur for a thin transmission or reflection grating. When light incident at an angle θ_r upon a holographic film of thickness d, which contains a Bragg grating with period Λ and slant angle ϕ, is diffracted by an angle θ_s, as shown in Fig. 13. In relation to Fig. 2, the tilt angle θ_{tilt} and the diffraction angle θ_{det} are taken to be positive and light propagates through this holographic optical element according to[7]

$$\theta_{tilt} = -\theta_{inc} \ , \tag{6.1a}$$

$$\sin\theta_{inc} = n\sin\theta_r \,, \tag{6.1b}$$

$$\sin\theta_s = \frac{\frac{\lambda}{n\Lambda}\cos\phi - \sin\theta}{\sqrt{1+\frac{\lambda(\lambda-\lambda_{BM})}{n^2\Lambda^2}}} \,, \tag{6.1c}$$

$$\sin\theta_{out} = n\sin\theta_s \,, \tag{6.1d}$$

$$\theta_{det} = \theta_{out} - \theta_{tilt} \,, \tag{6.1e}$$

where the parameters appearing in Eq. (6.1c) correspond to those of one of the Bragg gratings within the multiplex.[7] Equations (6.1b) and (6.1d) are Snell's law for each interface and Eq. (6.1c) relates the input angle θ_s to the diffraction angle θ_r for wavelengths of light that are not necessarily at the Bragg-matched wavelength λ_{BM}. The Bragg condition

$$\lambda_{BM} = 2n\Lambda\cos(\phi - \theta_r) \tag{6.2}$$

specifies the wavelength of light that is diffracted most efficiently, which occurs because the incident and diffracted waves are phase matched with the grating vector.

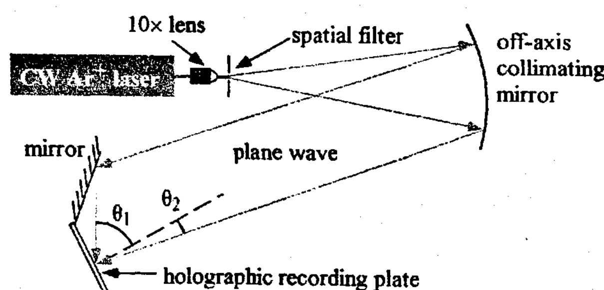

Fig. 14. Schematic drawing of the hologram recording station.

We write the Bragg gratings in the DuPont HRF 600X001-20 (20-μm thick) photopolymer using the interference pattern of two plane waves that are incident at angle θ_1 and θ_2. The experimental setup is shown schematically in Fig. 14. A large mirror designed for use with off-axis illumination collimates an argon-ion laser operating single line with a wavelength $\lambda_c = 514\,\text{nm}$. The portion of this large diameter beam that impinges directly upon the hologram recording plate is incident at an angle θ_2, and the other component, which is derived by reflection off the nearby flat mirror, is incident at an angle θ_1. Note that the rotation stages for the hologram recording plate and the flat mirror allow adjustment of these angles. For large angles of incidence, the grating spacing Λ will be small, whereas the grating spacing will be large for small angles of incidence. The angle ϕ at which the grating forms depends upon the mutual asymmetry in the angles of incidence with respect to the surface normal.

We evaluate the performance of the various holographic Bragg gratings formed in DuPont photopolymer film using a laser-based test station. A laser beam is normally incident upon the holographic element under test. The transmitted laser beam is diffracted owing to the presence of the Bragg grating. The transmitted power and angle of diffraction are measured. A single holographic optical element that contains four multiplexed Bragg gratings has been made and tested at four different wavelengths. As shown in Table 1, each Bragg grating diffracts its respective Bragg-matched wavelength at a different angle, where the diffraction angles are separated by 6°. These separate multiple outputs correspond to four different sensor bands.

TABLE 1 Performance measurements of diffraction by a hologram with four multiplexed Bragg gratings.

multiplexed hologram	reconstruction wavelength λ	diffraction angle θ_{out}	diffraction efficiency
S7M1	760.0 nm	42°	76%
S7M2	790.0 nm	48°	73%
S7M3	820.0 nm	54°	75%
S7M4	850.0 nm	60°	63%

7. CONCLUSIONS

We have considered a novel micro-opto-electro-mechanical (MOEM) device for wavelength division demultiplexing (WDDM) simultaneous signals coming from various sensors, which are each based upon fiber Bragg gratings. One great advantage of this MOEM device is only one single light source is required. The device design concept and its integration with the sensor system have been carefully illustrated. It shows that the feasibility of this MOEM tunable filter depends on the demonstration of two major components, a micro-deflector and a thin-film multiplexed volume hologram. The micro-deflector provides fast and repeatable adjustments to greatly enhance the dynamic tuning range of the filter. The thin-film multiplexed volume hologram in conjunction with photodetectors allows the tunable MOEM demultiplexer to operate at many simultaneous wavelength windows, i.e. multi-band operation.

To fabricate the micro-deflector, we developed a surface micromachining process that uses VLSI fabrication processes and a follow-up electroplating technique. In our process, we use thick photoresist as a sacrificial layer, by which the conventional VLSI fabrication process is modified as detailed in Sec. 4. Ten micro-deflectors with different dimensions were fabricated on a Si substrate. Each device has a height of 20 μm, which is defined by the thickness of the sacrificial layer, a width of 300 μm, and lengths ranging from 300 to 1200 μm in increments of 100 μm. The thickness and shape of the fabricated micro-deflectors are determined by the detailed nature of the electroplating process. The electrostatic actuation of each micro-deflector is demonstrated by observing the reflected laser beam from the tip of the micro-deflector. A physical model is also presented to explain the electrostatic actuation.

We also investigated the multi-band operation of a thin-film volume hologram. The principle of the multi-band operation is based on the fact that Bragg gratings can be multi-recorded within a single thin-film volume hologram. In our process, the interference of two plane-wave laser beams is recorded within a thin-film of DuPont photopolymer. One single multiplexed volume holographic element has been made and tested, which illustrates the potential multi-band operation.

ACKNOWLEDGEMENTS

This research program was supported by BMDO and managed by the Edwards Air Force Base, SBIR Office.

REFERENCES

1. C. P. Jacobson, "Shipboard fiber optic sensors," Proceedings of the Armed Forces Communications and Electronics association Fiber Optics Conference, McLean, VA, 1994.
2. O. S. Wolbeis, *Fiber Optic and Chemical Sensors and Biosensors*, (CRC Press, Boca Raton, 1991), Vol. I and II.
3. B. M. Beadle, R. S. Weis and C. A. Norwood, "Radical strain-induced attenuation in plastic optical fiber," Opt. Eng. **35**, 1696–1699 (1996).
4. K. E. Petersen, "Dynamic micromechanics on silicon: Techniques and devices," IEEE Trans. Electron Devices, **ED-25**, 1241–1250 (1978).
5. S. P. Timoshenko and J. M. Gere, *Mechanics and Materials*, (Van Nostrand, New York, 1972), p. 516.
6. H. L. Anderson, Ed., *A Physicist's Desk Reference*, (AIP, New York, 1989), 2nd ed.
7. H. Kogelnik, "Coupled wave theory for thick hologram gratings," Bell Sys. Tech. J. **48**, 2909–2947 (1969).